

Structure, electronic, and vibrational properties of glassy Ga₁₁Ge₁₁Te₇₈: Experimentally constrained density functional study

I. Voleská,¹ J. Akola,^{2,3,4,*} P. Jónvári,⁵ J. Gutwirth,¹ T. Wágner,¹ Th. Vasileiadis,⁶ S. N. Yannopoulos,⁶ and R. O. Jones^{3,7}

¹*Department of General and Inorganic Chemistry, Faculty of Chemical Technology, University of Pardubice, Náměstí Československých legií 565, CZ-53210 Pardubice, Czech Republic*

²*Department of Physics, Tampere University of Technology, P. O. Box 692, FI-33101 Tampere, Finland*

³*Peter Grünberg Institut PGI-1, Forschungszentrum Jülich, D-52425 Jülich, Germany*

⁴*COMP Centre of Excellence, Department of Applied Physics, Aalto University, FI-00076 Aalto, Finland*

⁵*Research Institute for Solid State Physics and Optics, P. O. Box 49, H-1525 Budapest, Hungary*

⁶*Foundation for Research and Technology Hellas, Institute of Chemical Engineering Sciences, FORTH/ICE-HT, P. O. Box 1414, GR-26504 Patras, Greece*

⁷*German Research School for Simulation Sciences, Forschungszentrum Jülich, D-52425 Jülich, Germany*

(Received 13 July 2012; published 13 September 2012)

The atomic structure and electronic and vibrational properties of glassy Ga₁₁Ge₁₁Te₇₈ have been studied by combining density functional (DF) simulations with x-ray (XRD) and neutron diffraction (ND), extended x-ray absorption fine structure (EXAFS), and Raman spectroscopies. The final DF structure (540 atoms) was refined using reverse Monte Carlo methods to reproduce the XRD and ND data as well as Ge and Ga *K*-edge EXAFS spectra, while maintaining a semiconducting band gap and a total energy close to the DF minimum. The local coordination of Ga is tetrahedral, while Ge has twice as many tetrahedral as defective octahedral configurations. The average coordination numbers are Ga, 4.1, Ge, 3.8, and Te, 2.6. The chemical bonding around Ga involves Ga 4*s*, Ga 4*p*, Te 5*s*, and Te 5*p* orbitals, and the bond strengths show bonding close to covalent, as in Ge. There are fewer Te chains and cavities than in amorphous Te, and a prepeak in the structure factor at 1.0 Å⁻¹ indicates medium-range order of the Ga/Ge network. Density functional calculations show that contributions of Te-Te, Ga-Te, and Ge-Te bonds dominate the experimental Raman spectra in the 110–150 cm⁻¹ range.

DOI: [10.1103/PhysRevB.86.094108](https://doi.org/10.1103/PhysRevB.86.094108)

PACS number(s): 61.43.Dq, 63.50.Lm, 71.15.Pd

I. INTRODUCTION

Chalcogenide alloys form a family of materials with a wide spectrum of technological applications, and tellurium-based alloys make up an increasingly important part. In addition to infrared optical elements,¹ electrolytes for solid-state batteries,² and sensors for liquid³ and gas analysis,⁴ Te-based alloys are the basis of many phase-change materials that are used widely in optical storage devices. Nanosized bits in thin films of these materials show remarkably rapid and reversible transitions between the amorphous (*a*) and crystalline (*c*) states, whose different conductivities and optical properties allow the state to be identified.⁵ Many alloys have compositions along the GeTe-Sb₂Te₃ pseudobinary tie line, with Ge₂Sb₂Te₅ serving as prototype. Others have compositions close to the eutectic of Sb-Te binary alloys (70:30), and both families have been the subject of extensive experimental and theoretical study. The function of these materials cannot be understood without a detailed knowledge of their structures, and discussions of amorphous and liquid chalcogenide structures have been described in many papers, including Refs. 6–9.

Many phase-change materials contain elements of groups 14, 15, and 16, and it has been found that Ge and Ga, in particular, improve both the stability of the amorphous phase (increased crystallization temperature) and the speed of crystallization.¹⁰ The latter is the time-limiting step in the write-erase cycle, and there is growing interest in alloys of Ge and/or Ga with Sb and Te. We study here Ga₁₁Ge₁₁Te₇₈ (GGT), a Te-rich alloy containing equal parts of Ga and Ge. In addition to their interest in the context of phase-change materials,

Te-based alloys transmit far-infrared radiation, which has led to applications in optical fibers in, for example, telescopes used in the Darwin mission of NASA and ESA (a search for life in Earth-like planets outside the solar system).^{11,12} The spectra of molecules considered as essential for life (H₂O, O₂, CO₂, and O₃) can be identified in the wavelength range 6–18 μm, extending the frequency range accessible to Se-based alloys.¹³ Glass formation in the binary system Ge-Te is possible for compositions near GeTe₄, but the difference between the glass temperature *T_g* and crystallization temperature *T_x* (ΔT) is only 77 °C, and stable glasses cannot be prepared.^{13,14} The glassy domain in the Ga-Ge-Te system is limited to a small region centered on the GeTe₄-GaTe₃ pseudobinary line, and the alloy Ga₁₀Ge₁₅Te₇₅ is characterized by *T_g* = 172 °C and *T_x* = 285 °C (ΔT = 113 °C). Stable samples of optical quality can be prepared, and fibers can be drawn. Materials with this composition have an exceptionally broad IR window^{13,14} (cutoff at 28 μm) and provided the first rewritable memory in the thermally drawn fibers.¹⁵

We describe the experimental techniques [x-ray diffraction (XRD), neutron diffraction (ND), extended x-ray absorption fine structure (EXAFS), and Raman spectroscopies] in Sec. II A and the density functional (DF) and molecular dynamics (MD) simulations¹⁶ in Sec. II B. The DF structure is refined using reverse Monte Carlo (RMC) techniques to reproduce the experimental data, and the final structure is discussed in Sec. III. The frequencies of Raman-active vibrational modes have been calculated for numerous structural units, and these results are also discussed in Sec. III. Our concluding remarks follow (Sec. IV).

II. METHODS

A. Experiment

The sample preparation and the XRD and ND measurements were described previously.⁸ The XRD measurements were carried out at the BW5 high-energy beamline at Hasylab (Hamburg, Germany), and the Ge and Ga *K*-edge EXAFS spectra were measured in transmission mode at the X1 beamline of Hasylab using radiation obtained by a Si 111 double-crystal monochromator. The intensity of the monochromatic beam before and after the samples was measured by ionization chambers filled with a N₂-Ar mixture, and the spectra were measured in steps of 0.5 eV near the edge. The data acquisition time was weighted with wave number k , and the $\chi(k)$ signal obtained from $\mu(E)$ using the program VIPER.¹⁷ The ND measurements were carried out at the 7C2 diffractometer (LLB, Saclay, France) using neutrons of incident wavelength 0.71 Å. The raw data were corrected using standard procedures.

The Raman spectra were recorded with the 632.8 nm excitation of a He-Ne laser at low power (~ 100 W cm⁻²), in order to avoid irradiation-induced heating and photoinduced changes. Laser light was focused by a 50 \times objective, and the backscattered light was detected by a charge-coupled device (CCD) cooled to 140 K and analyzed by a triple monochromator (Jobin-Yvon T64000) operating in double subtractive mode. The spectral resolution for the Stokes-side Raman spectra was ~ 2 cm⁻¹, and measurements of a few minutes led to a satisfactory signal-to-noise ratio. Polarized (VV, vertical polarization of incident laser, vertical analysis of scattered light) and depolarized (VH, vertical polarization of incident laser, horizontal analysis of scattered light) scattering geometries were used. Calibration of the wave number scale to take account of possible shifts of the monochromator and the polarization response of the Raman system has been performed by measuring the (polarized) spectra of liquid CCl₄.

B. Calculations

The DF-MD simulations used the CPMD package¹⁸ with the revised Perdew-Burke-Ernzerhof (PBEsol) approximation¹⁹ for the exchange-correlation energy. The electron-ion interaction was described by scalar-relativistic ionic pseudopotentials of Troullier-Martins form²⁰ with valence configurations Ga, $4s^2 4p^1$, Ge, $4s^2 4p^2$, and Te, $5s^2 5p^4$. We use periodic boundary conditions with a single point ($\mathbf{k} = \mathbf{0}$) in the Brillouin zone, and the kinetic energy cutoff of the plane-wave basis set is 20 Ry. Temperature control is via a Nosé-Hoover thermostat (frequency of 800 cm⁻¹, chain length 4).²¹

GGT is simulated at the experimental density (0.029 atoms/Å³, 5.547 g/cm³) using 540 atoms (60 Ga, 60 Ge, and 420 Te) in a cubic cell of size 26.51 Å. The initial structure was generated by the reverse Monte Carlo method to reproduce the XRD and ND data and the EXAFS *K*-edge data for Ga and Ge. All bond types were allowed. A simulation of 50 ps was performed at 300 K using Car-Parrinello MD with a time step of 7 a.u. (0.169 fs), after which the potential energy of the relaxed structure had converged. Data were then collected over 20 ps at 300 K. The final structure

was optimized (at 0 K) with a convergence criterion on all components of the nuclear gradients of 1×10^{-4} a.u.

RMC refinement was performed on this DF-optimized structure using minimum interatomic distances of 2.35 (Ga-Te), 2.45 (Ge-Te, Te-Te), and 2.30 Å (Ge-Ge, Ge-Ga, and Ga-Ga). The maximum moves along each coordinate were for Ga, 0.04, Ge, 0.04, and Te, 0.025 Å, and coordination numbers were not constrained. Spurious bond angles near 60° often occur in RMC refinements, so the bond angle distributions (Te-Ga-Te, Te-Ge-Te, Te-Te-Te, Te-Te-Ge, and Te-Te-Ga) were constrained to be near those found in the original DF-MD structure. Refinement was continued until $\sim 10^5$ steps were accepted, and the total energy of the final structure was only 33.8 meV/atom higher than that of the original DF structure. This technique (experimentally constrained DF calculations) has been applied successfully to study the structures of the phase-change materials Ge₂Sb₂Te₅ (GST) (Ref. 22) and Ag_{3.5}In_{3.8}Sb_{75.0}Te_{17.7} (AIST) (Ref. 23).

The interpretation of the Raman spectra has been supported by a series of DF calculations for TeH-terminated atomic clusters found to occur in *a*-GGT. These calculations use the GAUSSIAN 09 program package.²⁴

III. RESULTS AND DISCUSSION

A. XRD, ND, and RMC analysis

The structure factors $S(Q)$ for ND and XRD are in excellent agreement with our calculations for the RMC-refined structure (Fig. 1). Both ND and XRD show halo patterns typical of disordered materials, and the oscillations extend beyond 10 Å⁻¹. The ND and XRD structure factors differ, because the neutron scattering lengths are largest for Ga and Ge, and x-ray scattering is strongest in Te. The prepeak at 1.0 Å⁻¹ in the ND structure factor is also visible as a threshold in the XRD and indicates medium-range order of the Ga/Ge network. It is reproduced by the calculations. A similar prepeak has been seen in *a*-Ge₁₅Te₈₅, where analysis of the partial structure factors showed that it arose from the GeTe network.²⁵ Excellent agreement is also found for the amplitude and phase of the Ge and Ga *K*-edge EXAFS spectra of glassy (*g*) GGT (Fig. 2), indicating that the local configurations around Ga and Ge and the corresponding bond distances are described well.

The Ga-Te, Ge-Te, and Te-Te partial distribution functions (PDFs) are shown in Fig. 3 for the DF-MD simulation at 300 K (relaxed from the initial RMC configuration) and the final RMC-refined structure (from the DF-optimized configuration). The latter comprises a single frame, so that noisy PDF curves are inevitable. The first PDF maxima in the DF-MD data are Ga-Te (2.63 Å), Ge-Te (2.65 Å), and Te-Te (2.83 Å) (see Table I). The RMC procedure leads to maxima that are consistent with the DF-MD structure, but with slightly lower peak thresholds. This is consistent with the tendency of DF calculations to overestimate bond lengths in chalcogenides,⁷ although our use of the PBEsol functional means that this effect is weaker here. Lower PDF thresholds are reflected in the coordination numbers (Fig. 3, insets), but this effect is very weak in the range appropriate for bond cutoffs (3.0–3.2 Å; see Table I). The resulting coordination numbers are listed in Table II. The Ga-Te PDF shows a clear first

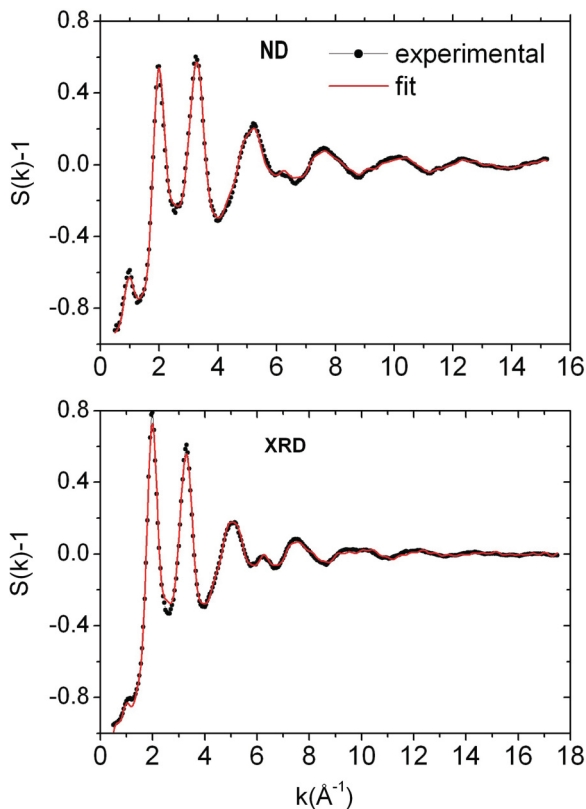


FIG. 1. (Color online) Experimental measurements of ND and XRD structure factors of glassy GGT (*g*-GGT) compared with the RMC-refined model (540 atoms).

minimum after 3.0 Å (tetrahedral coordination), but the broad minima in Ge-Te and Te-Te (nonzero values at 3.1–3.2 Å) can be traced to a defective octahedral local coordination.

The Te-Te PDF [Fig. 4(a)] shows that Te atoms have order up to 10 Å, as found in recent DF-MD simulations of *a*-Te.²⁶ The most pronounced features for GGT are a strong second-nearest-neighbor peak at 4.26 Å, maxima at 6.2, 7.9, and 9.9 Å, and a minimum at 5.3–5.4 Å. The peak heights of *a*-Te reflect the absence of other elements, and the shoulder at 3.5 Å arises from interchain distances. GGT shows long-range oscillations related to the Ga/Ge network. The partial coordination numbers of the Ga-Ga, Ga-Ge, and Ge-Ge bonds in Fig. 4(b) (0.07–0.17) show that these “wrong bonds” are not favored. The bond lengths (2.43–2.53 Å) are systematically smaller than for the PDF involving Te, and the well-defined PDF minima indicate that these bonds arise from tetrahedral configurations around Ga and Ge.

The coordination numbers (Table II) show small differences between the DF-MD simulation and the RMC-refined model, and the total coordination numbers N_{tot} are Ga, 4.1, Ge, 3.8, and Te, 2.6. Both Ga and Ge have near fourfold coordination, although the value for Ge suggests that some atoms have a defective octahedral environment with threefold coordination (3 + 3).^{7,27,28} The coordination of Te is higher than suggested by the “8 – N rule” (N is the number of valence electrons), as also found in elemental Te and $\text{Ge}_{15}\text{Te}_{85}$ in both liquid and amorphous phases.^{25,28} We note that these values depend on the radial cutoff chosen [Fig. 3].

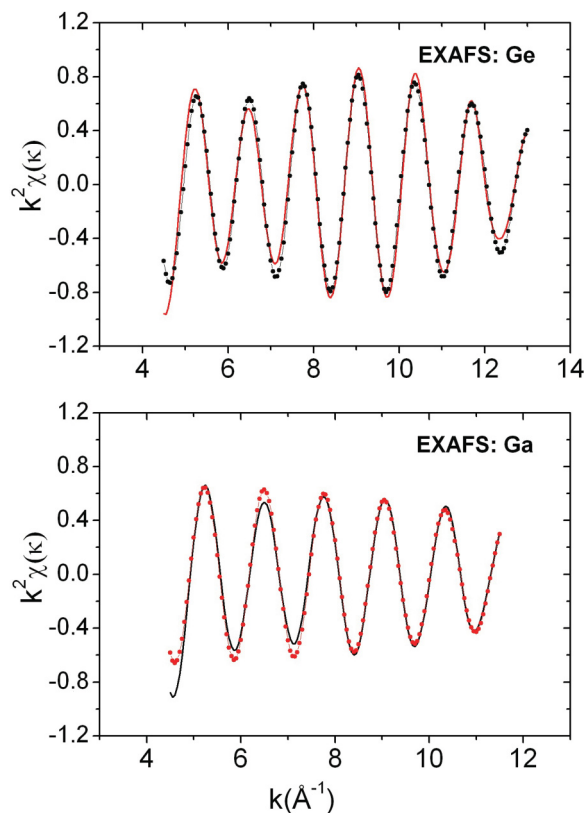


FIG. 2. (Color online) Experimental Ge and Ga *K*-edge EXAFS spectra of *g*-GGT compared with the RMC-refined model (540 atoms).

The angular distributions of Te-Te-Te, Te-Ge-Te, and Te-Ga-Te at 300 K are shown in Fig. 5 (DF-MD simulations). Together with Te-Te-Ge and Te-Te-Ga distributions (not shown), these angles have been used as constraints in the RMC refinement. Without angular constraints, RMC simulations can produce configurations with a broad scatter of bond angles and incorrect electronic properties, such as a vanishing band gap in a semiconductor.²² The angular distributions show several distinctive features: Te has a maximum at 95° and a smaller one near 180° corresponding to a defective octahedral environment, whereas the helical chains in *c*-Te have angles of 103.2° (2 + 4 coordination). Ga is peaked strongly at the tetrahedral value (109.5°), and Ge shows a broader maximum at 105° with extended tails on both sides. Triangular configurations lead to the weight around 60°. The broad Te-Ge-Te maximum and the bond angles above 150° indicate that some Ge atoms exist in defective octahedral environments. We have confirmed this by analyzing the fraction of “tetrahedral” atoms.²⁹ While 97.7% of Ga atoms are

TABLE I. The first maxima of the PDF at 300 K (in Å). The cutoff distances are given in parentheses.

	$R_{\text{max}}(\text{Ga})$	$R_{\text{max}}(\text{Ge})$	$R_{\text{max}}(\text{Te})$
Ga	2.43 (2.8)	2.49 (2.9)	2.63 (3.1)
Ge	2.49 (2.9)	2.53 (2.9)	2.65 (3.1)
Te	2.63 (3.1)	2.65 (3.1)	2.83 (3.2)

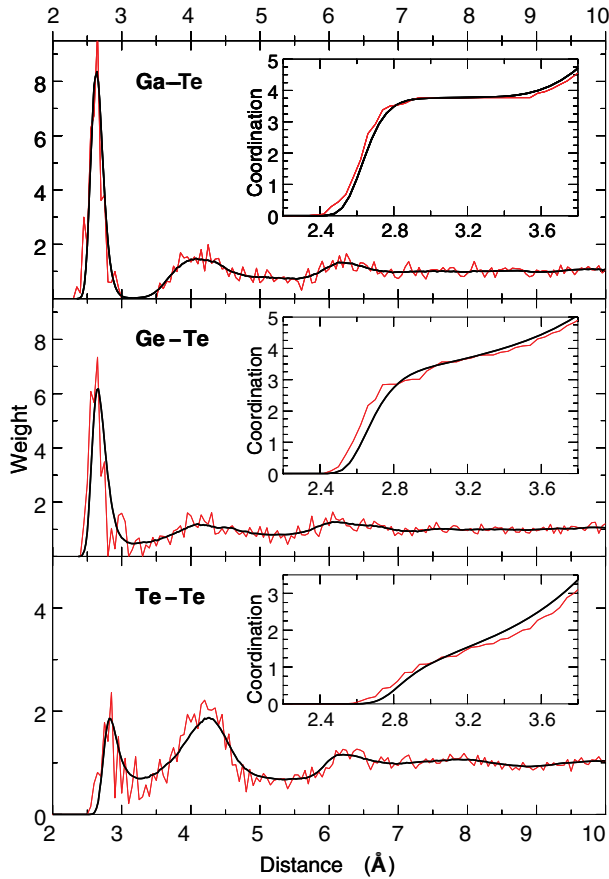


FIG. 3. (Color online) PDF of *g*-GGT for Ga-Te, Ge-Te, and Te-Te. Black, DF-MD simulation at 300 K (12 000 frames); red, RMC-refined structure (one frame). Insets: coordination numbers as a function of cutoff distance.

tetrahedral (thermal motion at 300 K causes small deviations from 100%), the number for Ge is 61.1%. The experimental Ge *K*-edge EXAFS spectrum (Fig. 2) is reproduced with this structure.

The nearest-neighbor analysis (Table III) provides further information about the local environment of *g*-GGT. Fourfold coordination dominates (99%) for Ga, while several coordination numbers occur for Ge and Te. The most common configurations are Ga-Te₄ (69.7% of Ga) and Ge-Te₄ (54.5% of Ge), while Te shows a wide scatter; twofold-coordinated Te-Te₂, Te-GeTe, and Te-GaTe configurations are the most abundant, but threefold configurations are important. Defective octahedral configurations of Ge are evident as GeTe₃ (23.3%) and GeTe₅ (3.3%), and there are no configurations with wrong bonds (with Ga or Ge) for these coordination numbers.

TABLE II. The average coordination of *g*-GGT at 300 K and in the RMC-refined model (in parentheses). The corresponding cutoff distances are listed in Table I.

	N_{Ga}	N_{Ge}	N_{Te}	N_{tot}
Ga	0.17 (0.17)	0.14 (0.14)	3.77 (3.77)	4.07 (4.08)
Ge	0.14 (0.14)	0.07 (0.07)	3.55 (3.57)	3.75 (3.77)
Te	0.54 (0.54)	0.51 (0.51)	1.52 (1.54)	2.57 (2.59)

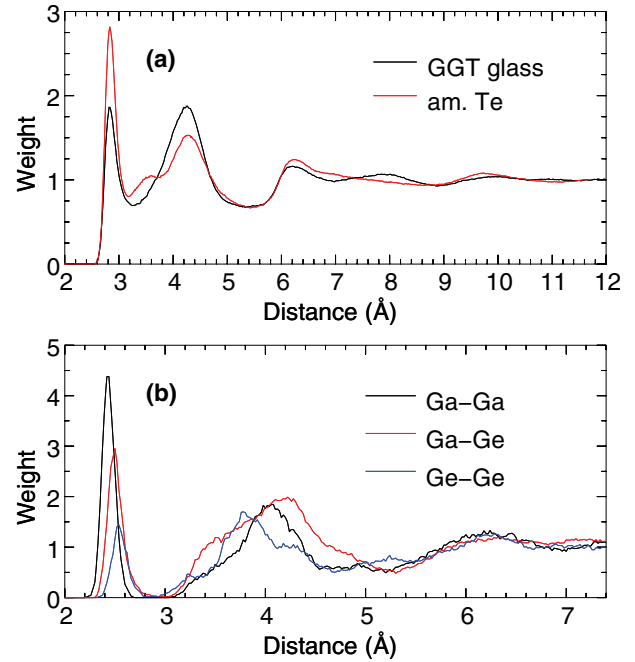


FIG. 4. (Color online) PDF of *g*-GGT: (a) Comparison of Te-Te PDF with DF-MD results for *a*-Te (Ref. 26), (b) PDF for Ga-Ga (black), Ga-Ge (red), and Ge-Ge (blue) for the MD simulations at 300 K. The corresponding coordination numbers are small (“wrong bonds”).

Figure 6 shows *g*-GGT from several perspectives. The two classes of Ge (tetrahedral and octahedral) have different color codes, and tetrahedral configurations around Ga and Ge are shown as polyhedra. Te atoms can be classified according to their participation in the Ga/Ge network, as was recently done in *a*-Ge₁₅Te₈₅.^{25,28} The Ga/Ge network is shown in Fig. 6(d), and the remainder, i.e., Te atoms not bonded to Ga or Ge, is shown in Fig. 6(e). The fraction of Te atoms not participating in the network (28%) is much less than in *a*-Ge₁₅Te₈₅ (52%).²⁵

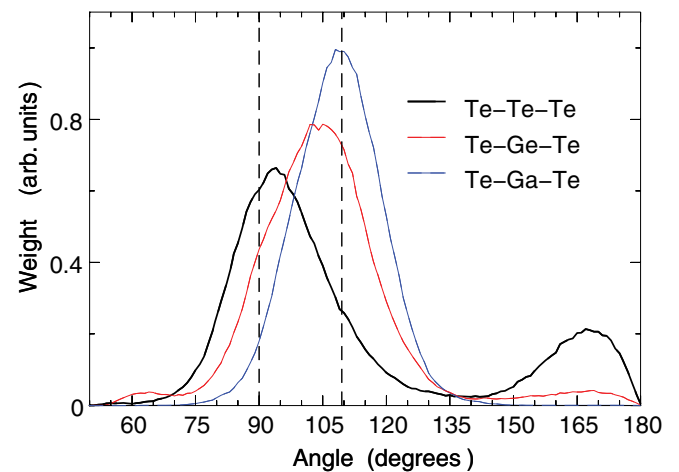


FIG. 5. (Color online) Angular distribution functions of *g*-GGT at 300 K (DF-MD simulation): Te-Ga-Te, Te-Ge-Te, and Te-Te-Te configurations. The dashed lines denote the octahedral (90°) and tetrahedral (109.47°) reference values.

TABLE III. Nearest-neighbor analysis of *g*-GGT at 300 K (DF-MD simulations): percentage of the atoms of the element with given configuration (with weights greater than 1%).

	1	2	3	4	5
Ga			<1	99	
				Te ₄ : 69.7	
				GaTe ₃ : 16.1	
				GeTe ₃ : 13.3	
Ge	<1		24	72	4
			Te ₃ : 23.3	Te ₄ : 54.5	Te ₅ : 3.3
				GaTe ₃ : 10.5	
				GeTe ₃ : 5.0	
				GaGeTe ₂ : 1.7	
Te	<1	51	43	6	<1
	Te ₂ : 16.0	GaTe ₂ : 9.7	Te ₄ : 1.6		
	GeTe: 12.6	Te ₃ : 9.3	GeTe ₃ : 1.2		
	GaTe: 12.3	GeTe ₂ : 9.0	GaGeTe ₂ : 1.1		
	GaGe: 6.6	GaGeTe ₂ : 6.4			
	Ge ₂ : 1.9	Ga ₂ Te: 2.7			
	Ga ₂ : 1.3	GaGe ₂ : 2.2			
		GeTe ₂ : 1.8			
		GaGe ₂ : 1.0			

These atoms form atoms, dimers, short chainlike segments, and branched fragments and do not segregate into Te-rich regions.

Cavities have been analyzed by determining regions that are farther from any atom than a cutoff distance 2.8 Å,⁷ and

the total volume is 19%–20% of the total. The same procedure yields 23% and 27% for *a*-Ge₁₅Te₈₅ and Te, respectively.^{25,26} The cavity volume decreases as the Ge/Ga content is increased and the atomic connectivity increases.

The calculated electronic densities of states (DOS) of *g*-GGT and *a*-Te are shown in Fig. 7(a). GGT is a small-band-gap (0.39 eV) semiconductor, as is bulk Te.²⁶ The valence states of Te comprise two bands with *s* and *p* character, respectively, with a large gap between −9 and −5 eV, and the *p* band is split into two subsets (−3 eV) due to chain formation. The presence of Ga and Ge introduces states in the band gap, and the splitting of the *p* band disappears. The projected DOS [Fig. 7(b)] shows that the new states at −8 and −6 eV have mainly 4*s* contributions from Ge and Ga, respectively, with some weight from Te. Analysis of the inverse participation ratios (not shown) shows that these states are strongly localized. The changing shape of the *p* band in GGT is consistent with the absence of long Te chains, since most Te atoms participate in the Ga/Ge network, and the overall coordination of Te is higher.

The presence of Ga leads to changes in the chemical bonding found in Ge_{*x*}Te_{1−*x*} alloys.^{25,28} There is no gap between the Ga 4*s* states and the *p* band, since these states have both Te 5*s* and Te 5*p* character. The chemical bond orders of Ga-Te, Ge-Te, and Te-Te bonds are plotted as a function of distance in Fig. 8. The values for Ga-Te and Ge-Te bonds are very similar (0.7–0.8) and close to that for a single covalent bond (1). Since Te-Te bonds have comparable values, the system can be described as “near covalent.” The

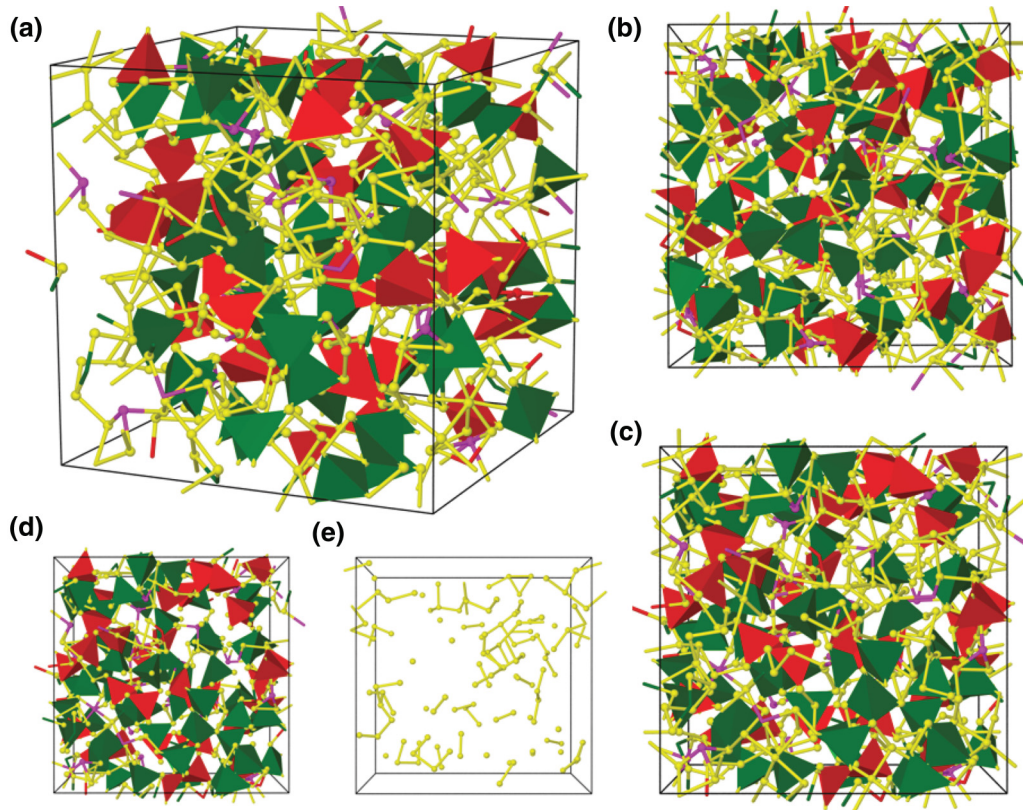


FIG. 6. (Color online) Glassy GGT: (a)–(c) From three perspectives, (d) atoms in Ga/Ge network (side view), and (e) Te atoms not bonded to Ga/Ge network (side view). Color code: Ga, green polyhedra; Ge (tetrahedral), red polyhedra; Ge (defective octahedral), magenta; and Te, yellow.

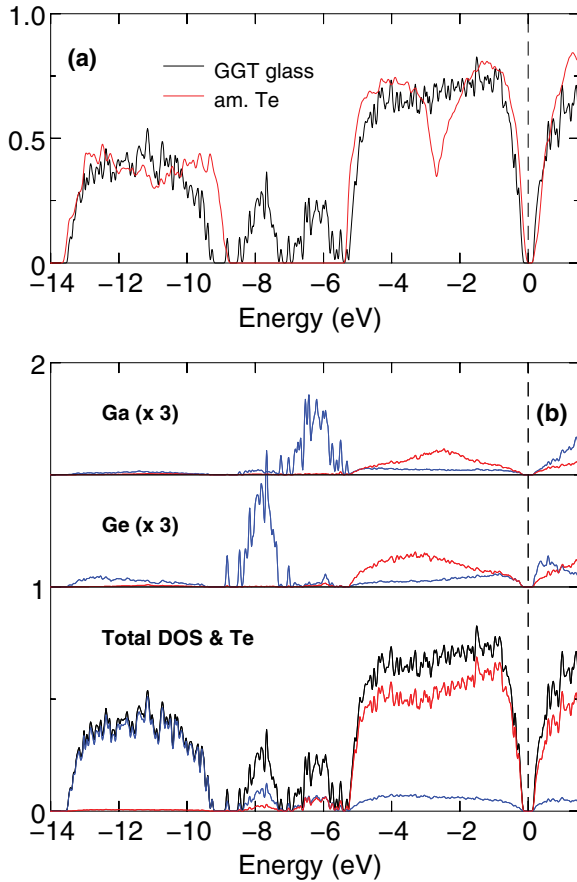


FIG. 7. (Color online) (a) Density of states of *a*-Te (Ref. 6) and *g*-GGT. (b) Projected density of states (DOS) of *g*-GGT. Blue, *s*, and red, *p* components. The scales for the Ga and Ge components are three times larger than for Te to compensate for the lower concentration.

coexisting Ge environments are reflected as two branches in the bond orders, where the bonds associated with tetrahedral Ge correspond to shorter distances and have a negligible contribution between 3.0 and 3.5 Å. This overlaps with the Ga-Te data. The continuum of values in Te-Te bond orders reflects the distorted octahedral environment, where the degree of distortion varies, as for threefold-coordinated Ge.

B. Vibration frequencies, Raman spectra

The power spectra (vibrational density of states) of *g*-GGT and *a*-Te at 300 K, and their projections onto the elements, were calculated from the Fourier transform of the velocity-velocity autocorrelation function and are shown in Fig. 9. They do not include infrared or Raman weights, which can change the signal shape considerably, as shown for GeTe by Mazzarello *et al.*³⁰ GGT frequencies have a plateau between 100 and 200 cm^{-1} and a threshold up to 250 cm^{-1} , which are the highest stretching modes of tetrahedral Ga and Ge configurations. These modes are reflected in the Te projection at higher frequencies, which is quite different from the case of *a*-Te.

Figure 10 shows that the unpolarized experimental Stokes-side Raman spectra of *c*-Te and *g*-GGT are very similar; the latter has broader peaks and is redshifted by $\sim 3 \text{ cm}^{-1}$ from *c*-Te. The Raman spectrum of *c*-Te shows strong bands at ~ 124

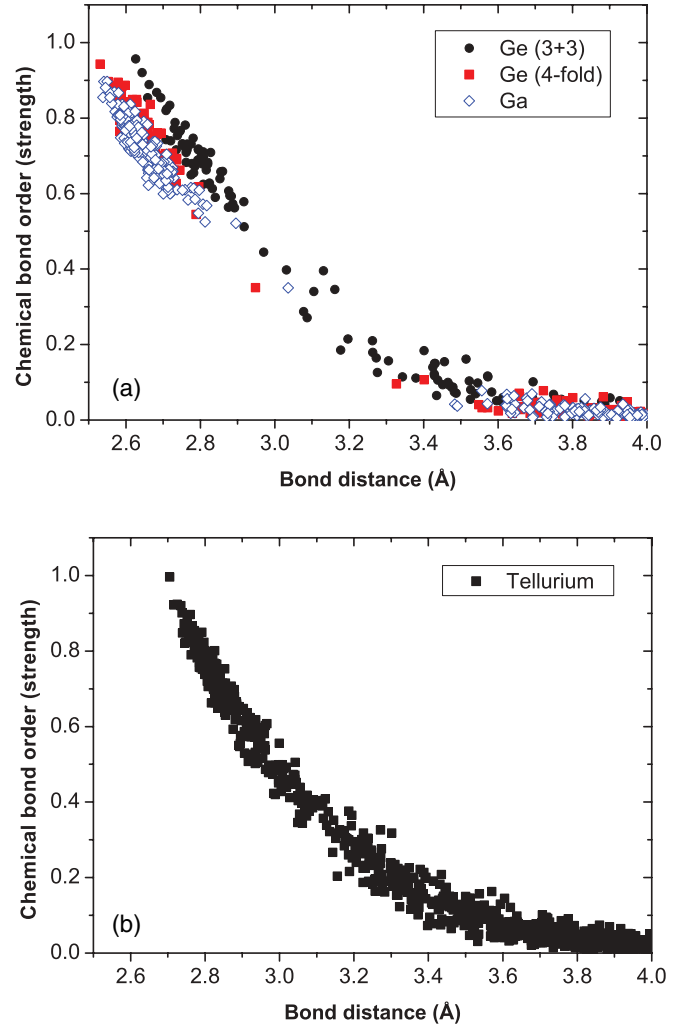


FIG. 8. (Color online) (a) Chemical bond orders (strengths) as a function of distance for (a) Ga-Te and Ge-Te bonds, and (b) Te-Te bonds.

and 144 cm^{-1} and a weaker one at $\sim 95 \text{ cm}^{-1}$. As shown by Pine and Dresselhaus,³¹ the strong peaks originate from the A_1 (124 cm^{-1}) and E_{TO} (144 cm^{-1}) modes, while the weaker peak arises from E_{TO} (95 cm^{-1}). The interpretation of the Raman spectra of *g*-GGT is not straightforward, since stretching vibrational frequencies of Te-Te, Ge-Te, and Ga-Te bonds are similar. The main vibrational mode (symmetric stretching or breathing mode) of the $\text{GeTe}_{4/2}$ tetrahedra overlaps strongly with the corresponding band of the $\text{GaTe}_{4/2}$ tetrahedra, due to the similar masses and bond strengths (see above) of Ge-Te and Ga-Te bonds. The symmetric stretching mode of the $\text{GeTe}_{4/2}$ tetrahedra is in the range 115–125 cm^{-1} ,³² i.e., near the A_1 mode of *c*-Te. The main Raman band of vapor-deposited *a*-Te is at $\sim 157 \text{ cm}^{-1}$.³³ Despite having many vibrational modes (see Fig. 9), the Raman spectrum of GGT is very weak in the range 150–180 cm^{-1} . This may be because the structure of *g*-GGT, with $\text{Ge}(\text{Ga})\text{Te}_{4/2}$ species separated by short Te_n chains ($n \leq 3$), differs from that *a*-Te.

Insight into the interpretation of the Raman modes of GGT can be obtained from DF calculations on Ga-Ge-Te clusters representative of the glass structure. The harmonic frequencies

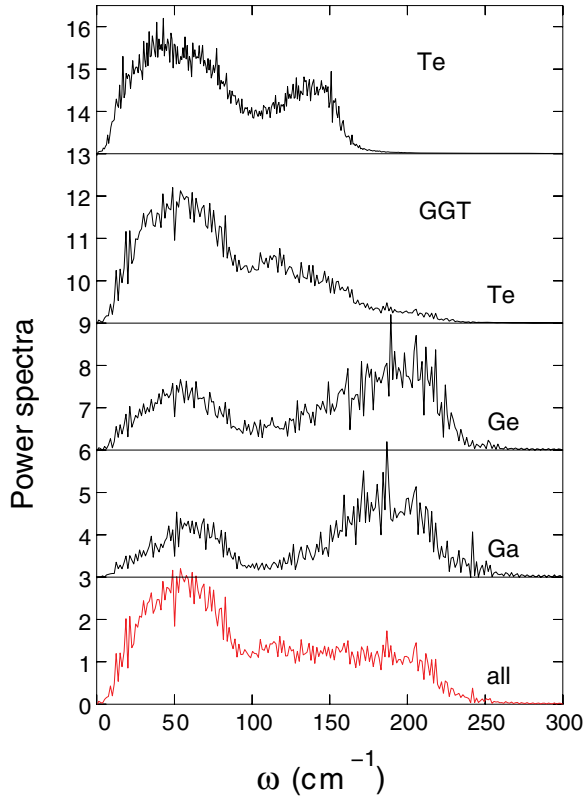


FIG. 9. (Color online) Vibrational density of states of *a*-Te at 300 K (top frame, Ref. 26) and of *g*-GGT at 300 K with projections onto elements. All curves have the same maximum.

of the optimized structures (Fig. 11) were calculated using IR and Raman weights and those with significant Raman activity are given in Table IV.

A quantitative analysis of the Raman spectra is necessary to compare the experimental data and the calculated harmonic frequencies. We use the reduced representation, which considers the distortion of the measured spectra caused by the finite sample temperature and the wavelength dependence of the scattered light. The reduced Raman spectrum represents the vibrational density of states weighted by the Raman coupling coefficient. The Stokes-side reduced Raman intensity (I_{red}) is related to the experimental value (I_{expt}) via

$$I_{\text{red}}(\nu) = (\nu_0 - \nu)^{-4} \nu [n(\nu, T) + 1]^{-1} I_{\text{expt}}(\nu), \quad (1)$$

where $n(\nu, T) = [\exp(h\nu/k_B T) - 1]^{-1}$ is the Bose occupation number, and h and k_B are the Planck and Boltzmann constants,

TABLE IV. Selected Raman-active vibrational modes for Ga-Ge-Te clusters shown in Fig. 11 (with terminating H atoms). Mixed modes indicate coupled Ga-Te, Ge-Te, and Te-Te vibrations.

Cluster	Formula	ν/I	ν/I	ν/I
a	GeTe ₃ (TeH) ₃	182/25.0 (Ge-Te)	202/53.0 (Ge-Te)	
b	GaTe ₄ (TeH) ₄	119/15.3 (Ga-Te)	164/40.2 (mixed)	
c	GeTe ₄ (TeH) ₄	126/24.2 (Ge-Te)	178/35.9 (Te-Te)	
d	Ga(TeH) ₃ Te ₂ TeH	120/20.4 (Ga-Te)	148/25.1 (mixed)	153/121.9 (mixed)
e	Ge(TeH) ₃ Te ₂ TeH	130/31.2 (Ge-Te)	180/19.6 (Te-Te)	
f	Ga(TeH) ₃ Te ₃ Ge(TeH) ₃	118/15.3 (Ga-Te)	127/13.3 (Ge-Te)	184/118.9 (Te-Te)
g	Ge(TeH) ₃ Te ₃ Ge(TeH) ₃	131/50.0 (Ge-Te)	171/2.5 (Te-Te)	179/14.87 (Te-Te)
h	Ge(TeH) ₃ Te ₄ Ge(TeH) ₃	129/86.1 (Ge-Te)	163/5.3 (mixed)	178/48.3 (Te-Te)

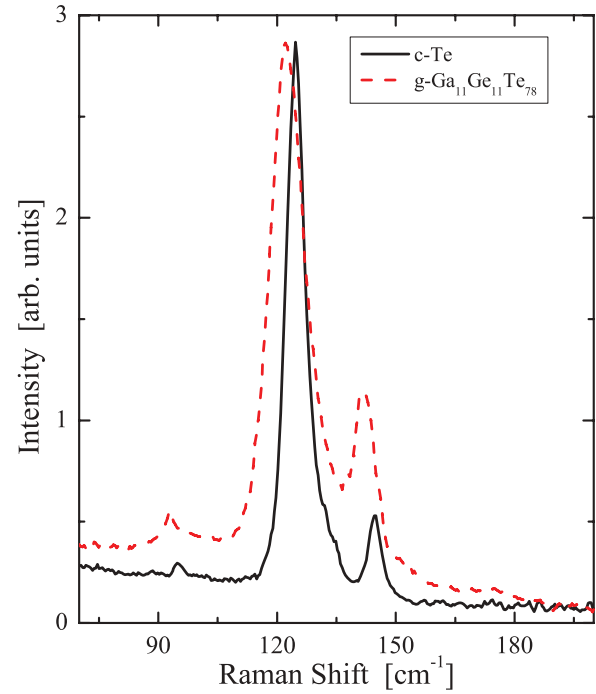


FIG. 10. (Color online) Unpolarized Stokes-side Raman spectra of *g*-GGT and *c*-Te.

respectively. The fourth-order term is the correction for the wavelength dependence of the scattered intensity, ν is the Raman shift in cm^{-1} , and ν_0 is the wave number of the incident radiation. Figure 12(a) shows the *reduced isotropic* and *anisotropic* spectra [$I_{\text{iso}} = I_{\text{VV}} - (4/3)I_{\text{VH}}$; $I_{\text{aniso}} = I_{\text{VH}}$] and the frequency dependence of the depolarization ratio ($\rho = I_{\text{VH}}/I_{\text{VV}}$). The isotropic part stands for the purely vibrational component of the normal modes arising from the diagonal elements of the polarizability tensor, and the minimum of ρ at $\sim 122 \text{ cm}^{-1}$ indicates that this frequency is the most polarized. Figure 12(b) illustrates a decomposition of the reduced isotropic spectrum into various Raman lines emerging from different species. A small number (eight) of Gaussian lines provides a satisfactory fit to the experimental data.

DF calculations of the clusters in Fig. 11 indicate that the broad, weak bands at 74 and 100 cm^{-1} are associated with bending and/or deformation modes of the structural units and their linkages, and the bands at 117 and 130 cm^{-1} originate from bond stretching (breathing modes) of GaTe_{4/2} and GeTe_{4/2} tetrahedral units, respectively. The corresponding

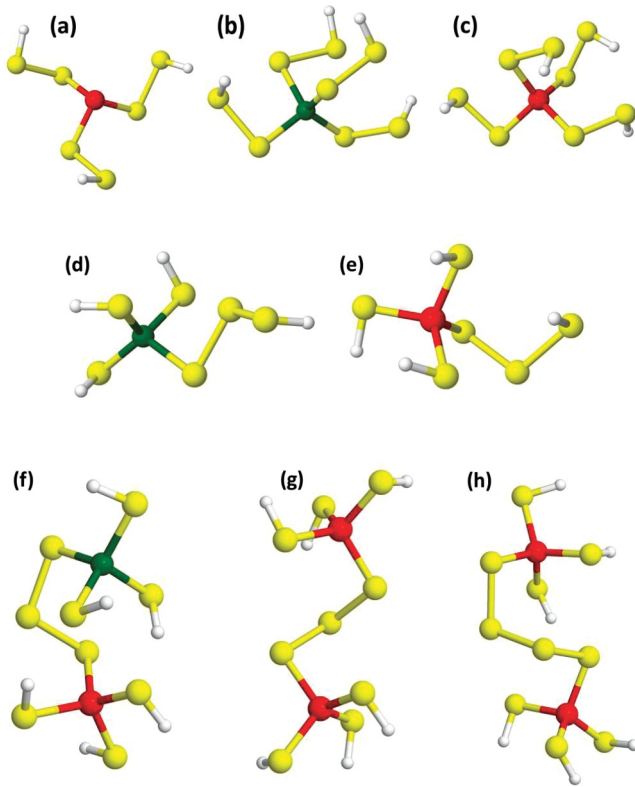


FIG. 11. (Color online) DF-optimized geometries of selected Ga-Ge clusters with H termination. The labels correspond to Table IV.

DF values (128 and 133 cm^{-1}) represent breathing modes of isolated $\text{Ga}(\text{TeH})_4$ and $\text{Ge}(\text{TeH})_4$ tetrahedra. The addition of an extra coordination sphere of Te atoms to the above units, i.e., $\text{Ga}(\text{TeTeH})_4$ and $\text{Ge}(\text{TeTeH})_4$ [Figs. 11(b) and 11(c) and Table IV] brings the calculated frequencies (119 and 126 cm^{-1}) closer to experimental values. The ratio of the experimental intensities (areas) I_{117}/I_{130} (0.52) is in reasonable agreement with the calculated value (0.63). The larger clusters (d)–(h) show similar Raman-active frequencies for the Ga-Te and Ge-Te bond stretches. The calculated frequency for the planar $\text{GaTe}_3(\text{TeH})_3$ is at 131 cm^{-1} (not shown), while the pyramidal $\text{GaTe}_3(\text{TeH})_3$ [Fig. 11(a)] shows several active modes at 182–202 cm^{-1} . The experimental peak at $\sim 176 \text{ cm}^{-1}$ can thus be associated with the distorted octahedral GeTe_3 units, which according to the DF-MD simulations represent $\sim 23\%$ of the local coordination of Ge. However, the simulations show few GaTe_3 sites, so the experimental Raman features cannot be assigned to them. The extended plateau between 148–184 cm^{-1} in the measured Raman spectra is in the same range as Raman-active modes of isomers (d)–(h) with Te-Te or mixed character.

IV. CONCLUDING REMARKS

The structure of glassy $\text{Ga}_{11}\text{Ge}_{11}\text{Te}_{78}$ has been studied by combining DF-MD simulations and experimental measurements using RMC refinement. The resulting model of 540 atoms satisfies all criteria for excellent agreement between theory and experiment (structure factors, EXAFS signals, DF energy, band gap). The local coordination of Ga and

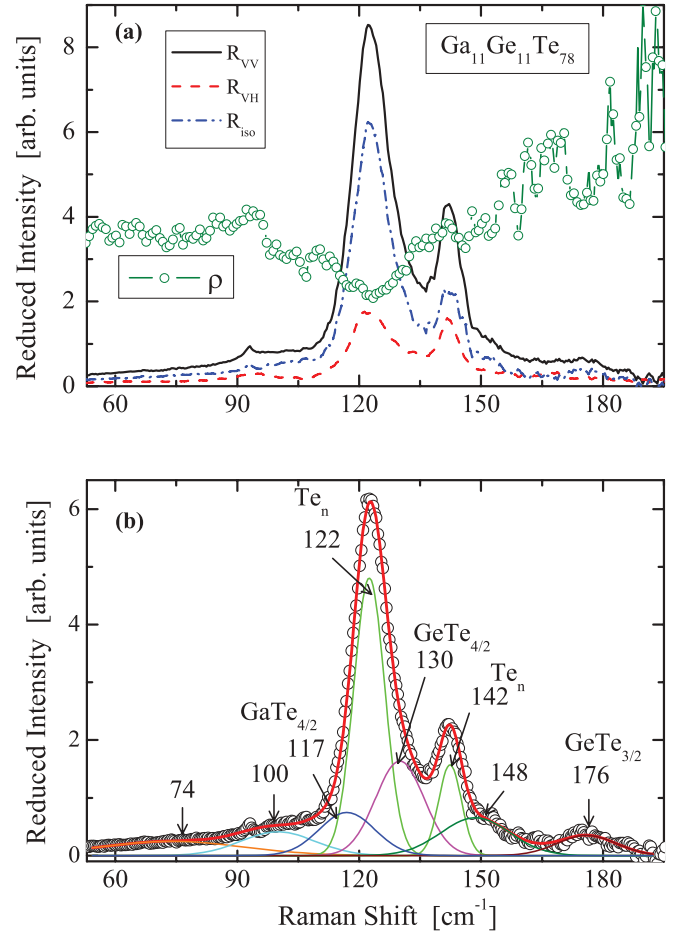


FIG. 12. (Color online) Reduced Raman spectra of *g*-GGT. (a) Polarized and isotropic $[I_{VV} - (4/3)I_{VH}]$ Raman spectra and frequency dependence of the depolarization ratio ρ . (b) Decomposition of the reduced isotropic spectrum.

Ge is predominantly tetrahedral, while Ge has coexisting defective octahedral configurations (three- or fivefold, 28%). The average coordination numbers, based on integration to the PDF minima, are Ga, 4.1, Ge, 3.8, and Te, 2.6. The prepeak in the structure factor at 1.0 \AA^{-1} indicates medium-range order of the Ga/Ge network (Fig. 6) similar to that in *a*- $\text{Ge}_{15}\text{Te}_{85}$, but the fraction of Te atoms not participating in the network is lower (28%). Te atoms form single atoms, dimers, short chainlike segments, and branched fragments, and there is no segregation into Te-rich regions. There are fewer cavities than in *a*-Te, but the total volume (19%–20%) is significantly higher than in some chalcogenides (e.g., 6% in *a*-GeTe).

The GGT structure we find is a semiconductor with a band gap of 0.39 eV. Such band gaps are often underestimated in DF calculations, and the bond angle constraints used during RMC refinement were chosen to favor a band gap. The overall DOS profile is similar to that of *a*-Te, but the presence of Ga and Ge adds states in the gap between the valence σ and π bands, and the π -band splitting is absent (fewer Te chains). The chemical bonding around Ga is a mixture of Ga 4*s*, Ga 4*p*, Te 5*s*, and Te 5*p* orbitals, while the chemical bond strengths are near covalent, as in Ge. The tetrahedral and distorted octahedral

coordination of Ge is visible in the bond order plots as two separate branches [Fig. 8(a)].

The Raman-active peaks of *g*-GGT at 125 and 145 cm^{-1} (Figs. 10 and 12) show significant contributions from GaTe_4 and GeTe_4 units, and the associated Raman-active breathing modes of Ga-Te and Ge-Te bonds are between 117 and 130 cm^{-1} for the tetrahedral local environment of Ga and Ge. The minimum of the measured depolarization ratio ρ at $\sim 122 \text{ cm}^{-1}$ indicates that this is the most polarized frequency. There is more weight at frequencies above 150 cm^{-1} than in *c*-Te, due to the presence of lighter elements. DF calculations for a selection of Ga-Ge-Te clusters show that there are several Raman-active modes in this region.

The experimentally constrained DF method has provided convincing structural information for the amorphous materials GST (Ref. 22) and AIST (Ref. 23). The approach has now been applied to a Te-rich alloy containing Ga and Ge, a member of an alloy family with great promise for phase-change memory and far-infrared optical applications. We are convinced that it will prove valuable in other contexts.

ACKNOWLEDGMENTS

The calculations were performed on IBM Blue Gene/P and Intel Xeon computers in the Forschungszentrum (FZ) Jülich with grants from the FZ Jülich and the John von Neumann Institute for Computing (NIC). J.A. acknowledges financial support from the Academy of Finland through its Centres of Excellence Program (Project No. 251748). S.N.Y. thanks G. Voyiatzis for providing the Raman facility at FORTH/ICE-HT. We are grateful for financial support from the Grants No. CZ.1.07/2.3.00/20.00254 “Research Team for Advanced Non-crystalline Materials” and No. CZ.1.07/2.3.00/30.0021 “Strengthening of Research and Development Teams at the University of Pardubice,” realized by the European Social Fund and Ministry of Education, Youth and Sports of the Czech Republic within the Education for Competitiveness Operational Program. The German Research School for Simulation Sciences is a joint venture of the FZ Jülich and RWTH Aachen University.

*jaakko.akola@tut.fi

¹A. Zakery and S. R. Elliott, *J. Non-Cryst. Solids* **330**, 1 (2003).

²E. Robinel, B. Carette, and M. Ribes, *J. Non-Cryst. Solids* **57**, 49 (1983).

³S. Marian, D. Tsuliani, T. Marian, and H. D. Liess, *Pure Appl. Chem.* **73**, 12 (2001).

⁴J. Kloock, L. Moreno, A. Bratov, S. Huachupoma, J. Xu, T. Wagner, T. Yoshinobu, Y. Ermolenko, Y. Vlasov, and M. Schöning, *Sens. Actuators, B* **118**, 149 (2006).

⁵See, for example, G. W. Burr, M. J. Breitwisch, M. Franceschini, D. Garetto, K. Gopalakrishnan, B. Jackson, B. Kurdi, C. Lam, L. A. Lastras, A. Padilla, B. Rajendran, S. Raoux, and R. S. Shenoy, *J. Vac. Sci. Technol. B* **28**, 223 (2010).

⁶J. Akola, R. O. Jones, S. Kohara, T. Usuki, and E. Bychkov, *Phys. Rev. B* **81**, 094202 (2010).

⁷J. Akola and R. O. Jones, *Phys. Rev. B* **76**, 235201 (2007).

⁸P. Jónvári, I. Kaban, B. Bureau, A. Wilhelm, P. Lucas, B. Beuneu, and D. A. Zajac, *J. Phys.: Condens. Matter* **22**, 404207 (2010).

⁹I. Kaban, T. Halm, W. Hoyer, P. Jónvári, and J. Neufeind, *J. Non-Cryst. Solids* **326**, 120 (2003); **327**, 120 (2003).

¹⁰L. van Pieterse, M. H. R. Lankhorst, M. van Schijndel, A. E. T. Kuiper, and J. H. J. Rosen, *J. Appl. Phys.* **97**, 083520 (2005).

¹¹L. Kaltenecker and C. V. M. Fridlung, *Adv. Space Res.* **36**, 1114 (2005).

¹²C. V. M. Fridlung, *Adv. Space Res.* **34**, 613 (2004).

¹³S. Danto, P. Houizot, C. Boussard-Plédel, X.-H. Zhang, F. Smektala, and J. Lucas, *Adv. Funct. Mater.* **16**, 1847 (2006).

¹⁴X. H. Zhang, L. Calvez, V. Seznec, H. L. Ma, S. Danto, P. Houizot, C. Boussard-Plédel, and J. Lucas, *J. Non-Cryst. Solids* **352**, 2411 (2006).

¹⁵S. Danto, Z. Ruff, Z. Wang, J. D. Joannopoulos, and Y. Fink, *Adv. Funct. Mater.* **21**, 1095 (2011).

¹⁶R. Car and M. Parrinello, *Phys. Rev. Lett.* **55**, 2471 (1985).

¹⁷K. V. Klementev, *J. Phys. D* **34**, 209 (2001).

¹⁸Computer code CPMD V3.13 (IBM Corporation, Armonk, NY, 1990–2010, MPI für Festkörperforschung, Stuttgart, 1997–2001); www.cpmd.org.

¹⁹J. P. Perdew, A. Ruzsinszky, G. I. Csonka, O. A. Vydrov, G. E. Scuseria, L. A. Constantin, X. Zhou, and K. Burke, *Phys. Rev. Lett.* **100**, 136406 (2008).

²⁰N. Troullier and J. L. Martins, *Phys. Rev. B* **43**, 1993 (1991).

²¹G. J. Martyna, M. L. Klein, and M. Tuckerman, *J. Chem. Phys.* **97**, 2635 (1992).

²²J. Akola, R. O. Jones, S. Kohara, S. Kimura, K. Kobayashi, M. Takata, T. Matsunaga, R. Kojima, and N. Yamada, *Phys. Rev. B* **80**, 020201(R) (2009).

²³T. Matsunaga, J. Akola, S. Kohara, T. Honma, K. Kobayashi, E. Ikenaga, R. O. Jones, N. Yamada, M. Takata, and R. Kojima, *Nat. Mater.* **10**, 129 (2011).

²⁴M. J. Frisch *et al.*, computer code GAUSSIAN09, revision A.1 (Gaussian, Inc., Wallingford, CT, 2009).

²⁵J. Kalikka, J. Akola, R. O. Jones, S. Kohara, and T. Usuki, *J. Phys.: Condens. Matter* **24**, 015802 (2012).

²⁶J. Akola and R. O. Jones, *Phys. Rev. B* **85**, 134103 (2012).

²⁷S. Caravati, M. Bernasconi, T. D. Kühne, M. Krack, and M. Parrinello, *Appl. Phys. Lett.* **91**, 171906 (2007).

²⁸J. Akola and R. O. Jones, *Phys. Rev. Lett.* **100**, 205502 (2008).

²⁹Fourfold-coordinated Ge atoms are “tetrahedral” if the average deviation of the six bond angles (for bonds $\leq 3.0 \text{ \AA}$) from the octahedral values (90° and 180°) exceeds 10° .

³⁰R. Mazzarello, S. Caravati, S. Angioletti-Uberti, M. Bernasconi, and M. Parrinello, *Phys. Rev. Lett.* **104**, 085503 (2010).

³¹A. S. Pine and G. Dresselhaus, *Phys. Rev. B* **4**, 356 (1971).

³²K. S. Andrikopoulos, S. N. Yannopoulos, G. A. Voyiatzis, A. V. Kolobov, M. Ribes, and J. Tominaga, *J. Phys.: Condens. Matter.* **18**, 965 (2006).

³³M. H. Brodsky, R. J. Gambino, J. E. Smith, Jr., and Y. Yacoby, *Phys. Status Solidi B* **52**, 609 (1972).